Science of the Total Environment 712 (2020) 136574

Contents lists available at ScienceDirect

Science of the Total Environment

journal homepage: www.elsevier.com/locate/scitotenv

Quantitative evaluation of the antibacterial factors of ZnO nanorod arrays under dark conditions: Physical and chemical effects on *Escherichia coli* inactivation

Eunhoo Jeong [a,b,1], Chan Ul Kim [c,1], Jeehye Byun [a], Jiho Lee [a], Hyung-Eun Kim [a], Eun-Ju Kim [a,b], Kyoung Jin Choi [c], Seok Won Hong [a,b,*]

[a] Water Cycle Research Center, Korea Institute of Science and Technology (KIST), Hwarangro 14 gil 5, Seongbuk-gu, Seoul 02792, Republic of Korea
[b] Division of Energy and Environment Technology, KIST-School, University of Science and Technology, Seoul 02792, Republic of Korea
[c] School of Materials Science Engineering and KIST-UNIST Ulsan Center for Convergent Materials, Ulsan National Institute of Science and Technology (UNIST), Ulsan 44919, Republic of Korea

HIGHLIGHTS

- Antibacterial mechanism of ZnO nanorod (NR) arrays against *E. coli* was investigated.
- The morphological effect as mechanical rupture was predominant for *E. coli* inactivation.
- The inactivation by reactive oxygen species was 2nd major mechanism in the dark.
- The chemical inactivation by Zn^{2+} ions released from the arrays was insignificant.

GRAPHICAL ABSTRACT

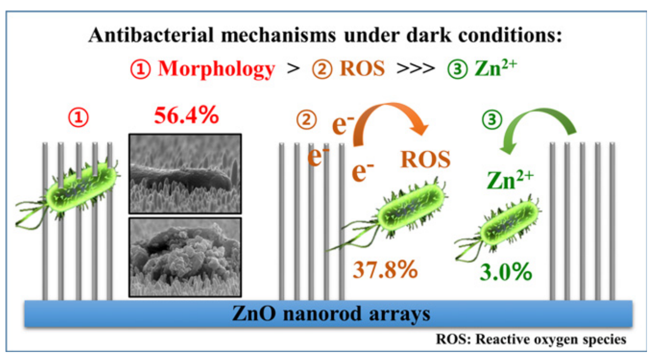

ARTICLE INFO

Article history:
Received 19 November 2019
Received in revised form 23 December 2019
Accepted 6 January 2020
Available online 8 January 2020

Editor: Kevin V. Thomas

Keywords:
Antibacterial mechanisms
Atomic layer deposition
Morphology
Reactive oxygen species
Zinc oxide nanorods

ABSTRACT

Although zinc oxide nanorod (ZnO NR) arrays are a nanomaterial that offers efficient bactericidal activity, they have not been systematically evaluated to quantitatively investigate their disinfection mechanism under dark conditions. In this study, ZnO NR arrays of different lengths (0.5–4 μm) were uniformly grown via hydrothermal synthesis. The longer arrays exhibited higher *Escherichia coli* (*E. coli*) inactivation efficiency up to 94.2% even under darkness for 30 min. When the NR arrays were coated via Al_2O_3 atomic layer deposition, the inactivation efficiency was decreased to 56.4% because the generation of reactive oxygen species (ROS) and the leaching of Zn^{2+} ions were both hindered by the surficial coverage of defect sites. The morphological effect, i.e., the mechanical rupture of *E. coli* on the surface, contributed 56.4% of the bactericidal efficiency; chemical effects, i.e., ROS formation and zinc ion release, contributed the remaining 37.8% under dark conditions. The bactericidal effect of fabricated ZnO NR arrays was further validated in bottled and pond water spiked with *E. coli*, exhibiting 87.5% and 80.4% inactivation efficiencies, respectively, within 30 min. Understanding these antibacterial mechanisms is not only of significance for research in this and related fields but also beneficial for potential application in various fields, e.g., biomedical and antifouling areas.

* Corresponding author at: Water Cycle Research Center, Korea Institute of Science and Technology (KIST), Hwarangro 14 gil 5, Seongbuk-gu, Seoul 02792, Republic of Korea.
E-mail address: swhong@kist.re.kr (S.W. Hong).

[1] These authors contributed equally to this work.

https://doi.org/10.1016/j.scitotenv.2020.136574
0048-9697/

1. Introduction

With rapid advances in nanotechnology, nanomaterials have enriched the field of water treatment by providing a variety of sorbents and catalysts (Belver et al., 2003; Colmenares and Luque, 2014; Shi and Zhang, 2016). One of the interesting applications of nanomaterials is their use as antimicrobial agents for water disinfection and microbial growth control. In particular, metal nanomaterials with different shapes—i.e., nanoparticles, nanotubes, nanorods (NRs), and nanowires—and compositions containing silver, zinc, iron, and copper have been studied to explore their antimicrobial activities (Chen et al., 2014; Osonga et al., 2016; Zhu et al., 2017). The main advantage of introducing nanomaterials for water disinfection is to prevent the production of harmful disinfection by-products (DBPs) (Li et al., 2008)

Among the nanomaterials, zinc oxide (ZnO) is known to be biocompatible and is thus widely used in biomedical applications (Huang et al., 2001; Keem et al., 2004). Since the antibacterial activity of ZnO was reported in the late 1990s (Jensen-Waern et al., 1998), various morphologies of ZnO nanomaterials have been investigated to examine the structural effects on bacterial inactivation. The semiconductive nature of ZnO, which has a band gap of 3.37 eV, has enabled photocatalytic degradation of organic pollutants in water under ultraviolet (UV) light illumination (Yi et al., 2019). Furthermore, ZnO exhibits substantial antibacterial efficiency even without a light source, and the bactericidal activity of ZnO has been suggested to be caused by the physical rupture of the bacteria on nanostructures (Lakshmi Prasanna and Vijayaraghavan, 2015).

However, Prasanna and Vijayaraghavan recently reported that surface defects such as oxygen defect sites often dominate the antibacterial behavior of ZnO nanoparticles (Lakshmi Prasanna and Vijayaraghavan, 2015). In particular, ZnO produced by hydrothermal synthesis is supposed to have surface defects of oxygen vacancies Vo^0, Vo^+, Vo^{2+} (0.05–3.1 eV) (Tam et al., 2006), where the oxygen vacancies of ZnO can serve as electron donors to provide electrons to the conduction band of ZnO (Liao et al., 2007). Therefore, even under dark conditions, reactive oxygen species (ROS) could be generated by the surface defect sites on ZnO (Hirota et al., 2010). The surface defects on ZnO nanoparticles, for instance, were found to perform a key role in the generation of ROS under dark conditions, which was confirmed by electron spin resonance (ESR) spectroscopy and scavenger studies (Lakshmi Prasanna and Vijayaraghavan, 2015). In addition, the dissolution of Zn^{2+} ions and the toxicity of ZnO itself have been lately proposed as potential factors in the antibacterial activity of ZnO (Lipovsky et al., 2011). Possible mechanisms of the antibacterial activity of ZnO in the dark can therefore be summarized as follows: (1) morphological effect for physical deformation, (2) ROS generation at oxygen defect sites, and (3) dissolution of Zn^{2+} ions. Although these physical and chemical factors are known to affect the bactericidal performance of ZnO, to the best of the authors' knowledge, quantitative evaluation of which mechanism is the most responsible has not been reported to date.

This study was designed to understand the mechanistic aspects of antibacterial activity of ZnO NR arrays against *E. coli* under dark conditions. The NR arrays were grown in different lengths from 0.5 to 4 μm via a hydrothermal method to observe the morphological effect on the antibacterial activity of ZnO. Then, in order to evaluate the chemical effects of ZnO in bactericidal activity, the surface of ZnO NR arrays was coated with Al_2O_3 (thicknesses of 15 and 30 nm) by atomic layer deposition (ALD). The efficiency loss after coating the surface could be deduced as the combined effect of ROS generation and released Zn^{2+} ions. Consequently, the relative physical and chemical factors in the antibacterial activity of ZnO NR arrays could be compared. Understanding the bacterial inactivation of ZnO NR arrays is of scientific significance for both ZnO-based nanostructures and practical water disinfection. The antibacterial activity of ZnO NR arrays with an optimum length was further evaluated using actual bottled and pond water, verifying the potential of ZnO NR arrays for an alternative inactivation technique.

2. Experimental section

2.1. Chemical reagents

Silicon wafer, zinc nitrate hexahydrate ($Zn(NO_3)_2 \cdot 6H_2O$), hexamethylenetetramine (HMTA, $(CH_2)_6N_4$), trimethylaluminum (TMA, Al $(CH_3)_3$), 5,5-dimethyl-1-pyrroline N-oxide (DMPO), isopropanol, Cr (VI), superoxide dismutase (SOD), zinc chloride ($ZnCl_2$), and zinc standard for inductively coupled plasma (ICP) were supplied by Sigma Aldrich (St. Louis, MO, USA) in analytical grades. All aqueous solutions were prepared with sterile distilled water. Luria–Bertani (LB) broth and LB agar were purchased from BD Difco, USA.

2.2. Fabrication of ZnO NR arrays

ZnO NR arrays were synthesized using methods reported in the literature (Vayssieres et al., 2001). The substrate for growing ZnO NR arrays was a (100) silicon wafer. For the nucleation of ZnO NRs, a 40 nm thick ZnO seed layer was first deposited on the substrate by sputtering. For further growth of the arrays, a hydrothermal reaction solution was prepared by mixing a 0.2 M HMTA solution and a 0.2 M zinc nitrate hexahydrate ($Zn(NO_3)_2 \cdot 6H_2O$) solution in a bottle with an autoclavable screw cap. The silicon substrate with a ZnO seed layer was immersed in the solution. The bottle was heated at 90 °C for the desired period to yield different lengths of NR arrays, where synthesis time variations of 2 h 15 min, 4 h 30 min, 9 h, and 18 h resulted in 0.5 μm, 1 μm, 2 μm, and 4 μm long arrays, respectively. Finally, the samples were washed with deionized water and dried in air. ALD (Lucida D100) of Al_2O_3 was performed using TMA and H_2O as reactants (Groner et al., 2004). During ALD of Al_2O_3, the TMA and H_2O precursor gases were injected into the ALD reactor in an alternating exposure sequence. One cycle was designed to purge TMA for 15 s after 0.2 s pulse, and then purge H_2O for 15 s after 0.2 s pulse. Average Al_2O_3 growth rates of 1.12 Å/cycle were obtained at 200 °C. The Al_2O_3 layers were grown on the ZnO NR arrays with film thicknesses of 15 and 30 nm.

2.3. Characterization of ZnO NR arrays

The morphology and structural characteristics of ZnO NR arrays were observed using field-emission scanning electron microscopy (Cold FE-SEM, S-4800, Hitachi High-Technologies, Japan). To investigate the surficial coating of aluminum oxide on arrays, a scanning transmission electron microscope (STEM, JEM-2100F, JEOL, Japan), and an energy dispersive spectrometer (EDS, JEM-2100F, JEOL, Japan) were utilized. Atomic force microscope (AFM) images of the ZnO were obtained using an Innova AFM (Bruker Corporation, France). Root mean square (RMS) roughness values were calculated based on $10 \times 10\ \mu m^2$ tapping-mode AFM scans. Electron spin resonance (ESR) spectroscopy (JES-X310, JEOL, Japan) was used to monitor the production of ROS from ZnO NR arrays. DMPO was used as a spin trapping agent to trap hydroxyl radicals, where DMPO was dropped onto the surface of the NR arrays and diluted to 10 mM with distilled water. An inductively coupled plasma-optical emission spectrometer (ICP-OES, Agilent 730 Series, Agilent Technologies, USA) was employed to quantify the Zn^{2+} ions released from the ZnO NR arrays.

2.4. Measurement of antibacterial activity of ZnO NR arrays

Escherichia coli (*E. coli*, KCTC2571), purchased from the Korean Collection for Type Culture (KCTC), was used for antibacterial activity testing. All the culture experiments were carried out inside an aseptic cabinet (Clean Bench J-CBWV1, JISICO Co., LTD, Korea). To measure the antibacterial activity on the ZnO NR array surface ($2 \times 2\ cm^2$), a drop-test method was used (Akhavan and Ghaderi, 2010), wherein 100 μL of the *E. coli* water solution (an initial concentration of 10^7 CFU/mL) was directly dropped onto the surface of ZnO NR arrays,

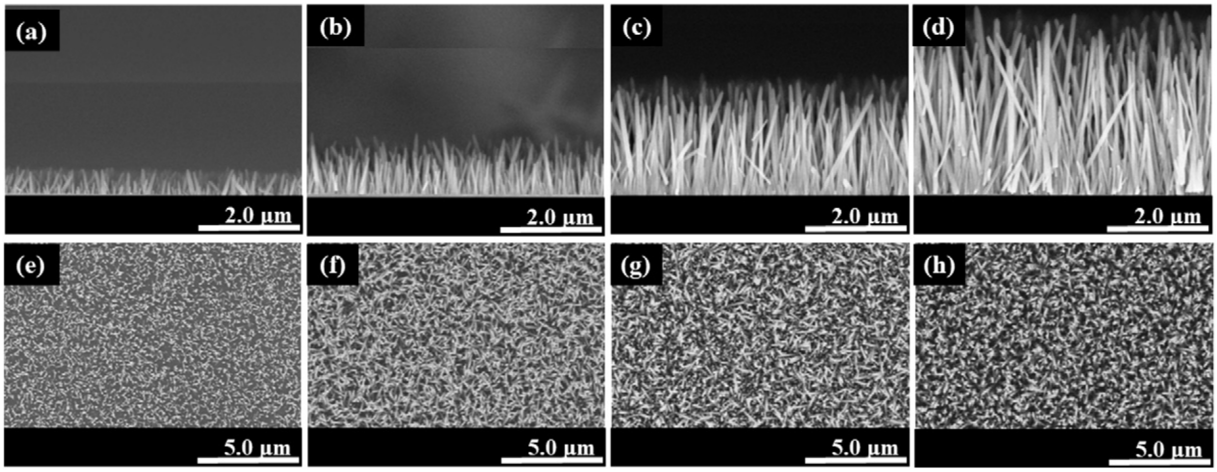

Fig. 1. Cross-sectional FE-SEM images of grown ZnO NR arrays on silicon wafer with the length of (a) 0.5 μm, (b) 1 μm, (c) 2 μm, and (d) 4 μm. The corresponding top-view FE-SEM images of the ZnO NR arrays with the growth length of (e) 0.5 μm, (f) 1 μm, (h) 2 μm, and (h) 4 μm at ×20,000 magnification.

which were pre-cleaned with ethanol. Experiments were conducted under different light conditions—specifically, dark, visible light ($\lambda =$ 490–625 nm, 4 W), or UV illumination (a black light blue lamp, $\lambda =$ 350–400 nm, 4 W)—for 30 min. After incubation for 30 min with light variation, antibacterial activity was measured via the spread plate method (Moriarty, 1998). Other detailed procedures are provided in the Supporting Information (SI) section.

The scavenger experiments were performed using individual scavengers of isopropanol (IPA), Cr(VI), and SOD to quench •OH, e^-, and $•O_2^-$, respectively. The concentrations of scavengers were $[IPA]_0 =$ 0.5 mM, $[Cr(VI)]_0 = 0.05$ mM, and $[SOD]_0 = 70$ mg/L. The relative viability equation is as follows (Eq. (1)):

$$\text{Inactivation efficiency } (\%) = \frac{C_0 - C_t}{C_0} \times 100 \quad (1)$$

where C_0 and C_t represent the initial number of colonies and those surviving at reaction time t, respectively. All values of inactivation efficiency are the average of triplicate measurements, and error bars represent the standard deviations of three repeated measurements, $^*P < 0.05$.

Additionally, the methods and equipment used to measure the water quality parameters are described in the SI section.

3. Results and discussion

3.1. Characterization of ZnO NR arrays

The morphology of ZnO NR arrays grown to different lengths is shown in Fig. 1. Fig. 1(a) illustrates the cross-sectional FE-SEM image of NR arrays after 2 h 15 min of reaction time, showing that the NR arrays grew uniformly on the substrate with an average length of 0.5 μm. When the hydrothermal synthesis reaction times increased to 4 h 30 min, 9 h and 18 h, as shown in Fig. 1(b)–(d), respectively, the lengths of ZnO NR arrays grew longer, to maximums of 1 μm, 2 μm, and 4 μm, respectively. The maximum length of NR was found to be 4 μm with 18 h of hydrothermal reaction. With respect to the increasing length of arrays, the surface density of NR became higher (Amin et al., 2011) as displayed in Fig. 1(a)–(h). Compared to the shortest 0.5 μm tall NR array, 1 μm and 2 μm tall arrays exhibited more dense packing of ZnO NR arrays, while the tallest 4 μm tall array showed similar density with 2 μm tall arrays (Fig. S1). With the aid of HMTA as a surfactant, the thickness of the NR arrays remained identical at 70 ± 10 nm regardless of the hydrothermal reaction time (Polsongkram et al., 2008). Such a variation in surface morphology of NR arrays would be a key consideration for the physical deformation of bacteria.

Surficial capping of ZnO NR arrays with Al_2O_3 layers was observed, as shown in Fig. 2. The STEM images clearly show that NR arrays were

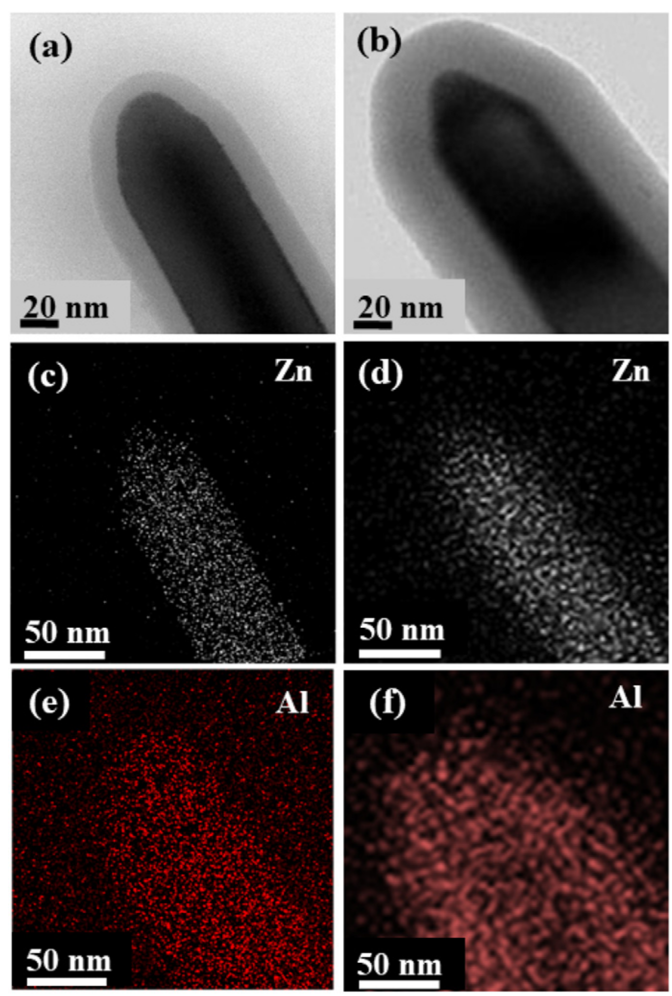

Fig. 2. STEM images of ZnO NR capped with (a) 15 nm and (b) 30 nm thick Al_2O_3 layer. EDS elemental mapping images of 15 nm coated NR for (c) Zn and (e) Al atoms, and of 30 nm coated NR for (d) Zn and (f) Al atoms.

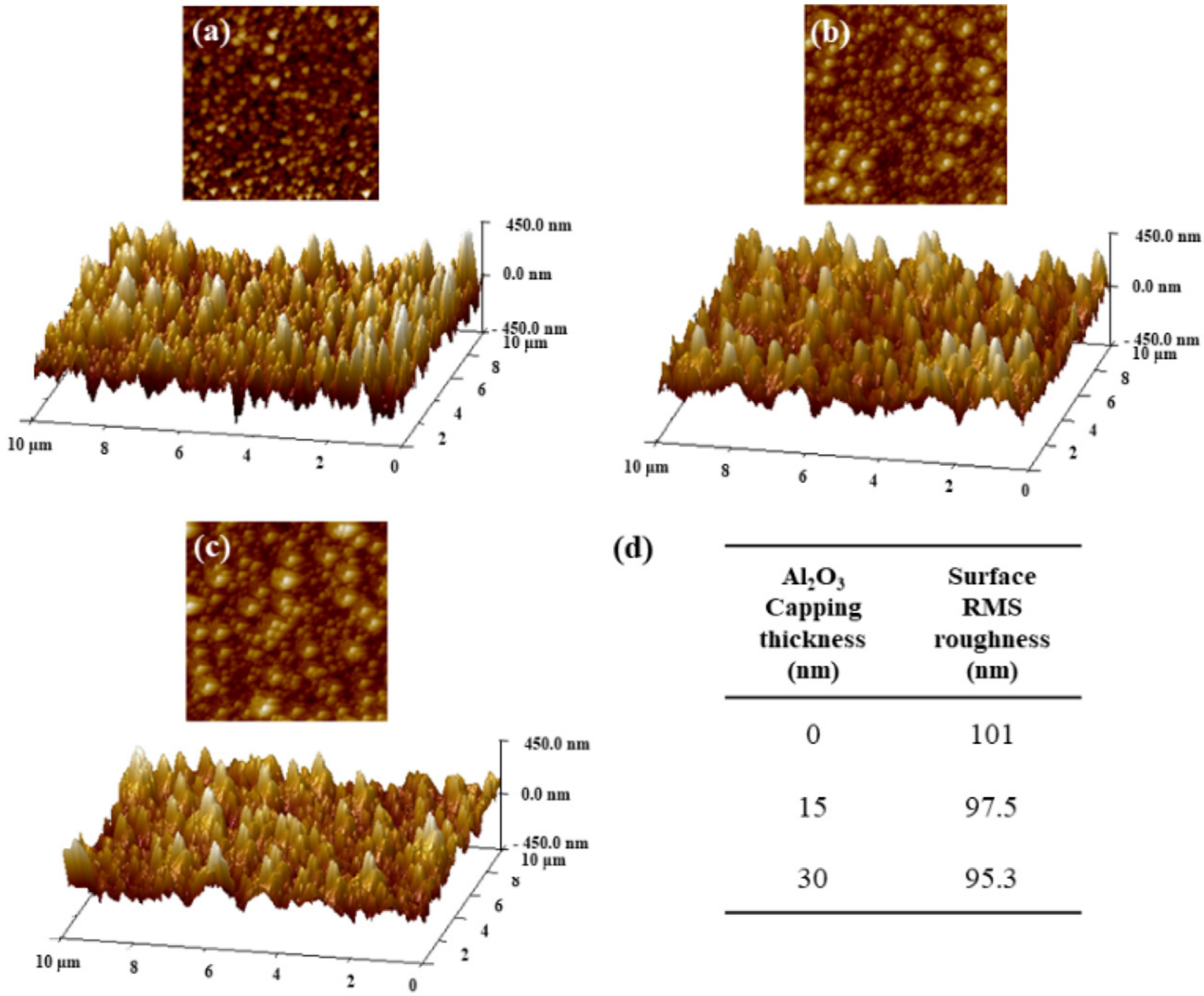

Al_2O_3 Capping thickness (nm)	Surface RMS roughness (nm)
0	101
15	97.5
30	95.3

Fig. 3. AFM surface images of 2 μm tall ZnO NR arrays (a) without Al_2O_3 capping, (b) with 15 nm thick Al_2O_3 capping, and (c) with 30 nm thick Al_2O_3 capping layers. (d) RMS roughness with Al_2O_3 capping layers thickness variation.

covered with a uniform layer of Al_2O_3, and the coating thickness could be controlled to be 15 and 30 nm without deforming the original NR arrays, as displayed in Fig. 2(a) and (b), respectively. The EDS elemental mapping images (Fig. 2(c)–(f)) show the spatial distributions of Zn and Al atoms, indicating confinement of ZnO with Al_2O_3 layers in different thicknesses. The Al_2O_3 layers on the NR arrays covered the defect sites of ZnO to prevent the possible chemical effect toward the bacterial inactivation. Despite the surficial coating, the density and the morphology of the arrays changed only minimally, as seen with the 2 μm tall arrays with and without Al_2O_3 layers (Fig. S2).

To further understand the effect of the Al_2O_3 layers on the morphology of the ZnO NR arrays, the surface of nanostructures was analyzed using AFM and roughness measurements. Fig. 3(a)–(c) show the AFM surface images of the uncoated and the coated arrays with 2 μm length, where the surface density of the NR arrays was not drastically influenced even with the thicker coating of 30 nm Al_2O_3 layer. In addition, the surface RMS roughness of the arrays before and after the surficial coating decreased from 101 to 95.3 nm (Fig. 3(d)), implying that the surface roughness of the arrays was maintained with the Al_2O_3 coatings without significant difference (George, 2009; Wenzel, 1949). The morphological attribute of the ZnO NR arrays were preserved even after the surficial coating, allowing us to differentiate the physical and the chemical effect for bacterial inactivation on the ZnO NR arrays. In other words, the uncoated arrays would hold the synergetic effect of morphology and chemistry from defect sites, while the coated arrays only show the morphological effect due to the coverage of defects.

3.2. Antibacterial activity of ZnO NR arrays with various lengths

Fig. 4 displays the inactivation efficiencies of ZnO NR arrays with the different lengths (0.5–4 μm) toward *E. coli* upon a 30 min exposure under different light conditions (dark, visible light, and UV irradiation). As the length of the ZnO NRs increased, the bactericidal efficiency clearly increased, for instance, showing 63.5% with 0.5 μm and 94.2% with 4 μm tall array under dark conditions. When the length of the arrays was shorter than 1 μm, the inactivation efficiency was more dependent on the type of light, where the 0.5 μm tall array showed c.a. 10% increase of bactericidal efficiency under UV light illumination to yield 73.1%. As for the ZnO, the wide band gap (~3.37 eV) readily absorbs UV light to generate ROS in the environment, thereby leading to the higher antibacterial activity of the arrays under the UV light illumination (Bagchi et al., 2018). Conversely, the 4 μm tall array exhibited similar antibacterial activities up to 96.2% regardless of the light conditions, implying that the morphological effect became dominant with the longer arrays. The high antibacterial efficiency over 90% was achieved when the ZnO NR arrays were longer than 2 μm even under dark conditions, which is highly comparable with the nanomaterials from previous reports (Table S1). It is worth noting that the ZnO NR arrays showed the quantitative inactivation efficiency in only 30 min, while other materials

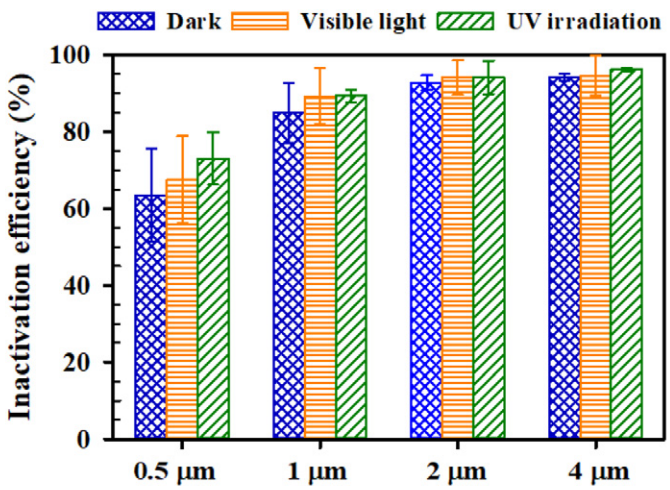

Fig. 4. Inactivation efficiency of *E. coli* upon 30 min exposure of ZnO NR arrays with different lengths (0.5–4 μm) under different conditions (dark condition, visible light, and UV irradiation).

shown in the previous studies have taken much longer times (1 h – 10 days) for a bactericidal efficiency similar to the ZnO NR arrays presented herein. In the following section, the morphological and chemical effects of ZnO NR arrays for bacterial inactivation are carefully investigated to identify the leading factors under dark conditions.

3.3. Morphological effect of ZnO NR arrays for bacterial inactivation

Fig. 5 shows the shape of dead *E. coli* stabbed by ZnO NR arrays of different lengths (0.5–4 μm) under dark conditions. Materials with sharp edges, such as nanoflakes and nanowires, have exhibited superior antibacterial effects owing to physical action (Akhavan and Ghaderi, 2011; Kaimlová et al., 2019). The sharp edges of the NR arrays cut through the *E. coli*'s cell membrane, resulting in a release of phospholipids and constituents from the cells (Bhadra et al., 2011; Ramani et al., 2013), finally leading to the death of *E. coli*. As described earlier (Fig. 4), the longer arrays result in higher bacterial inactivation (Akhavan et al., 2009). The 0.5 μm tall array was less dense, thereby providing less physical contact toward the *E. coli*. Furthermore, as shown in Fig. 5(a), NR (0.5 μm) was too short to penetrate the cell membrane of *E. coli*. Therefore, the bacteria remained on the surface of the ZnO NR array, not completely penetrated. However, the mechanical rupture of *E. coli* becomes more apparent when the length of the ZnO NR arrays reaches 1 μm (Fig. 5(b)). Fig. 5(c) and (d) more clearly show that the *E. coli* was deformed while releasing its constituents on the surface of the 2 and 4 μm tall ZnO NR array. The dense packing of long ZnO NRs provided the physical inactivation of *E. coli*, allowing a facile and rapid inactivation under dark conditions. As the bactericidal efficiency was saturated beyond the length of 2 μm, the following chemical effects by ZnO defect sites were mainly tested with the 2 μm tall ZnO NR array.

3.4. Effect of generated ROS from defects of NR arrays for bacterial inactivation

Previous studies have reported that ROS interferes with cell membrane phospholipids, lipoproteins, and nucleic acids, leading to oxidative stress and ultimately cell death (Applerot et al., 2009; Chandel et al., 2000). Therefore, generation of ROS from ZnO should be critical for the antibacterial activity of NR arrays. As shown in Fig. 6(a), 2 μm tall arrays generated hydroxyl radicals even in the dark condition monitored by ESR analysis. The arrays exhibited more intense formation of hydroxyl radicals under UV irradiation (Fig. 6(b)). When the 2 μm tall array was coated with Al_2O_3 layers in 15 nm thickness, there was slight evolution in ESR signal in both dark and UV conditions (Fig. 6(a) and (b)). With the thicker 30 nm layer, the ZnO NR array showed no noticeable response in ESR spectra neither under dark nor UV irradiation, indicating a complete coverage of detect sites on ZnO by the 30 nm thick Al_2O_3 layer, as shown in Fig. 6(a) and (b). As reported earlier, the oxygen vacancy on defect sites of ZnO transfers the electron to nearby surrounding molecular oxygen, forming superoxide radicals (Eq. (2)). Superoxide radicals react with water molecules to generate hydroperoxyl radicals (Eq. (3)) that further recombine to yield hydrogen peroxide molecules (Eq. (4)). The hydrogen peroxide molecules form hydroxyl ions and hydroxyl radicals by the reaction with superoxide radicals (Eq. (5)), thereby making the hydroxyl radicals detectable in the ESR spectra. Meanwhile, singlet oxygen ($^1O_2$) does not form under the dark condition owing to the lack of photo-generated holes (Hirota et al., 2010; Zhang et al., 2014; Yi et al., 2019).

$$O_2 + e^- \rightarrow {}^{\cdot}O_2^- \tag{2}$$

$$^{\cdot}O_2^- + H_2O \rightarrow {}^{\cdot}HO_2 + OH^- \tag{3}$$

$$^{\cdot}HO_2 + {}^{\cdot}HO_2 \rightarrow H_2O_2 \tag{4}$$

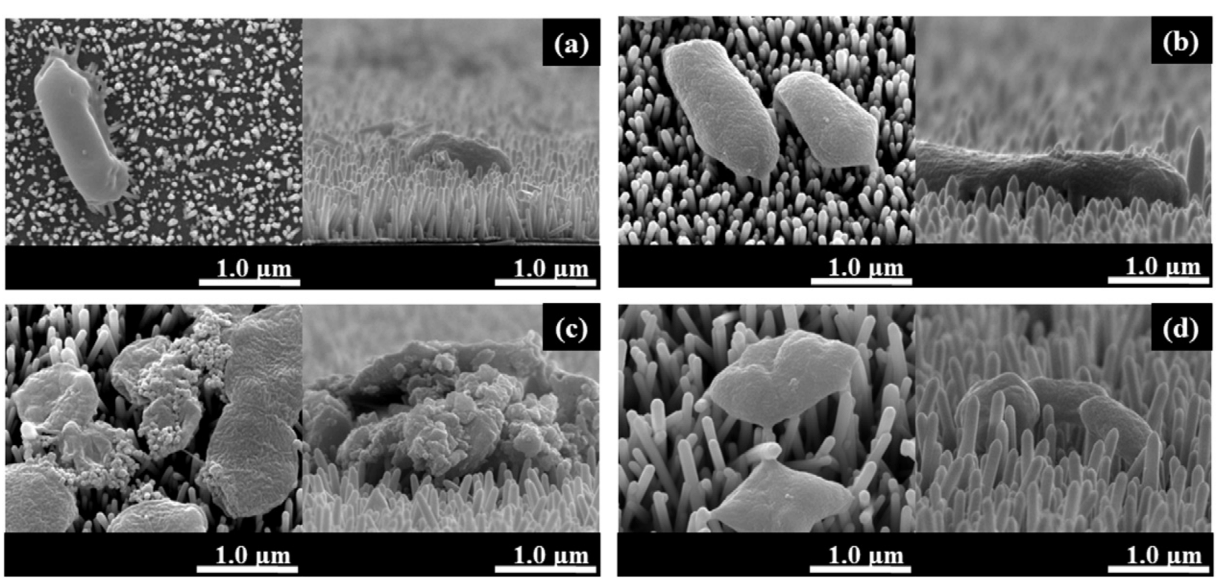

Fig. 5. Top-view FE-SEM images of ZnO NR array surface after inactivation of *E. coli* under dark conditions. The length of the arrays was (a) 0.5 μm, (b) 1 μm, (c) 2 μm, and (d) 4 μm.

$$H_2O_2 + {}^{\cdot}O_2^{-} \rightarrow O_2 + {}^{\cdot}OH + OH^{-} \quad (5)$$

With the detection of the ROS produced by the ZnO NR arrays in the dark, the effect of ROS in terms of antibacterial activity on the arrays was further examined using a series of radical scavengers (Fig. 6(c)). Isopropanol (IPA), Cr(VI), and SOD were used to quench hydroxyl radicals, free electrons (e^{-}), and superoxide radicals (Liu et al., 2016), respectively. The inactivation efficiency of 2 μm tall ZnO NR arrays was substantially decreased by adding radical scavengers, in which the quenching effect followed in the order of superoxide radical, free electron, and hydroxyl radical. In particular, the superoxide radical scavenger (i.e., SOD) showed the highest effect, reducing the bacterial inactivation efficiency down to 25.1% in comparison to 92.8% without the radical scavenger. As the superoxide radicals are known to be initially generated by the electron transfer from the defects of ZnO to the molecular oxygen under dark conditions (Lakshmi Prasanna and Vijayaraghavan, 2015), the scavengers of superoxide radicals and free electrons had the most effect. When the arrays were capped with the 15 nm thick Al_2O_3 layer, the inactivation efficiency decreased to 81.3%, implying less ROS formation due to the surficial coverage of defect sites. The bactericidal efficiency was further decreased by the addition of radical scavengers; the efficiency was reduced to 50.4 and 45.1% with free electron and superoxide radical scavengers, respectively, which is in line with the tendency observed for the uncoated arrays.

The thicker Al_2O_3 coating of ZnO NR arrays resulted in a considerable decrease of bactericidal efficiency down to 43.9%, although the morphology of nanostructures remained intact after the surficial coating, as shown in Fig. 2. The antibacterial efficiency of the 30 nm coated array was not affected in the presence of radical scavengers, indicating that the thick coverage of defect sites on ZnO completely hindered the ROS formation. Compared with using the uncoated and 15 nm coated arrays, not considering the morphological effect, the additional quenching experiments demonstrate that the lower antibacterial efficiency of the latter array resulted from the reduction of defect-induced ROS formation (Fig. S3(a) and (b)). Conversely, the 30 nm coated arrays in all lengths showed marginal dependency on radical scavengers (Fig. S3(c)), proving that the *E. coli* inactivation on the 30 nm coated array was solely attributed to the morphological effect for physical deformation of *E. coli*.

3.5. Effect of released Zn^{2+} ions for bacterial inactivation

It has been reported that zinc ions can bind to microbial membranes such as mammalian cells (Sugarman, 1983), thereby delaying the phase of the growth cycle to hinder complete cell division (Radke et al., 1994). The possible leaching of zinc ions from the ZnO NR arrays might contribute to the bacterial inactivation, as reported in earlier studies (Song et al., 2010; Joe et al., 2017). The measurement of the released kinetics Zn^{2+} ion from the ZnO NR arrays (2×2 cm^2) was performed under the same conditions as the drop-test. All results are expressed in terms of μg/mL/cm^2. Fig. S4 shows the kinetics of the zinc ions released from the 2 μm tall ZnO NR arrays and the Al_2O_3-capped arrays under dark and UV irradiation. Regardless of the lighting conditions, zinc ions were released from the uncoated ZnO NR arrays, showing ~13.2 μg/mL/cm^2 within 60 min of treatment in water. In contrast, the Al_2O_3-capped arrays with the coating thickness of 15 and 30 nm exhibited a far lower amount of zinc release under dark conditions, up to 2.1 and 0.9 μg/mL/cm^2, respectively. There was no drastic change in the zinc concentration released

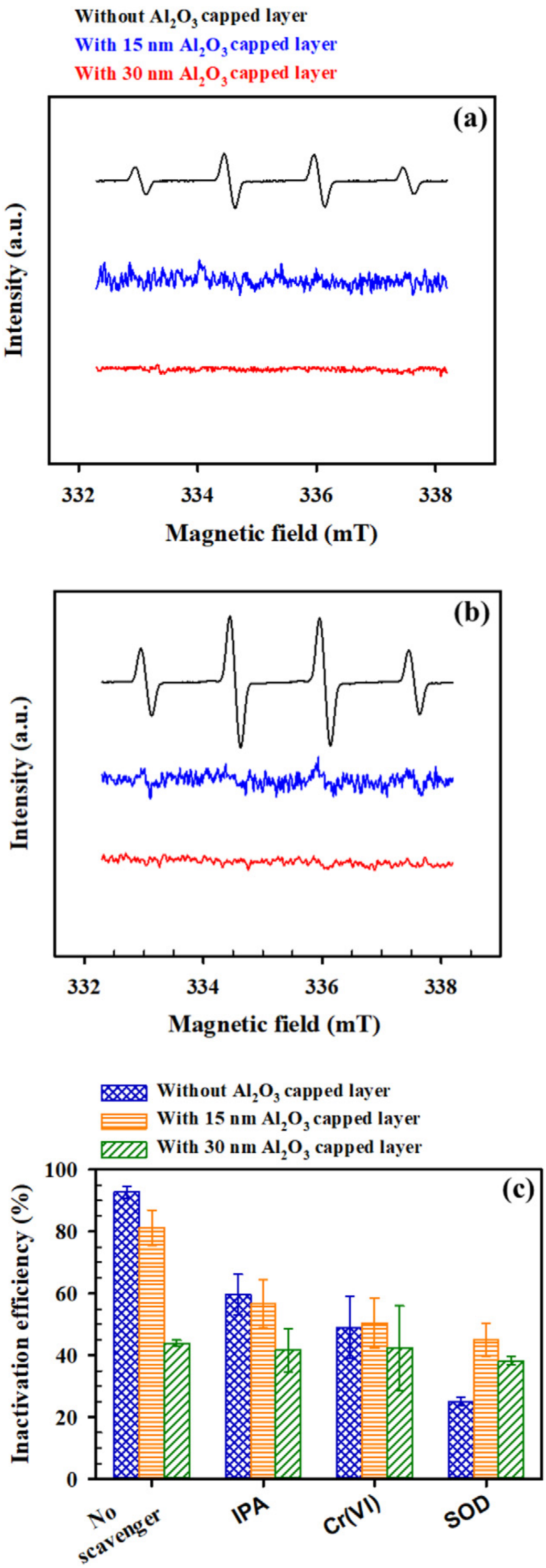

Fig. 6. ESR analysis of •OH radicals generated from 2 μm tall ZnO NR arrays under (a) dark and (b) UV illumination. (c) ROS scavenging experiments of 2 μm tall ZnO NR arrays and the Al_2O_3-capped arrays under dark conditions. Scavengers isopropanol (IPA), Cr(VI), and superoxide dismutase (SOD) were used to quench •OH, e^{-}, and $•O_2^{-}$, respectively.

from the coated arrays even under UV irradiation. Through the surficial coating of ZnO NR arrays, the leaching of zinc ions could be highly suppressed by one-fifth relative to that from the uncoated arrays. According to the released zinc concentration, the control experiment for *E. coli* inactivation was conducted in an aqueous zinc solution within the range from 1 to 20 μg/mL. As shown in Fig. S5, the inactivation of *E. coli* was negligible even in the high zinc amount of 20 μg/mL, yielding only 3% bactericidal effect. Considering that the zinc ions were released from the ZnO NR arrays at a maximum rate of 16.3 μg/mL/cm^2, the effect of zinc ions from the arrays was less significant for bacterial inactivation. This finding is in agreement with the results of a previous report, stating that a Zn^{2+} concentration of 100 mg/L can cause cell death (Jiang et al., 2016). As the coated arrays released insignificant amounts of zinc ions, the share of zinc ions in antibacterial activity on the Al_2O_3-capped arrays was very minor.

The leaching of zinc ions from ZnO NR arrays may lead to structural deformation of the arrays. The release of zinc ions from the 2 μm tall ZnO NR array was monitored over 30 cycles (Fig. S2(c)). The average zinc release was found to be ca. 12.0 μg/mL/cm^2, indicating that 0.02% of Zn leached from the array throughout the cycles. Nevertheless, the morphology of the ZnO NR arrays was not damaged, even after the 30th cycle (Fig. S6), and the antibacterial activity remained intact (Fig. S7).

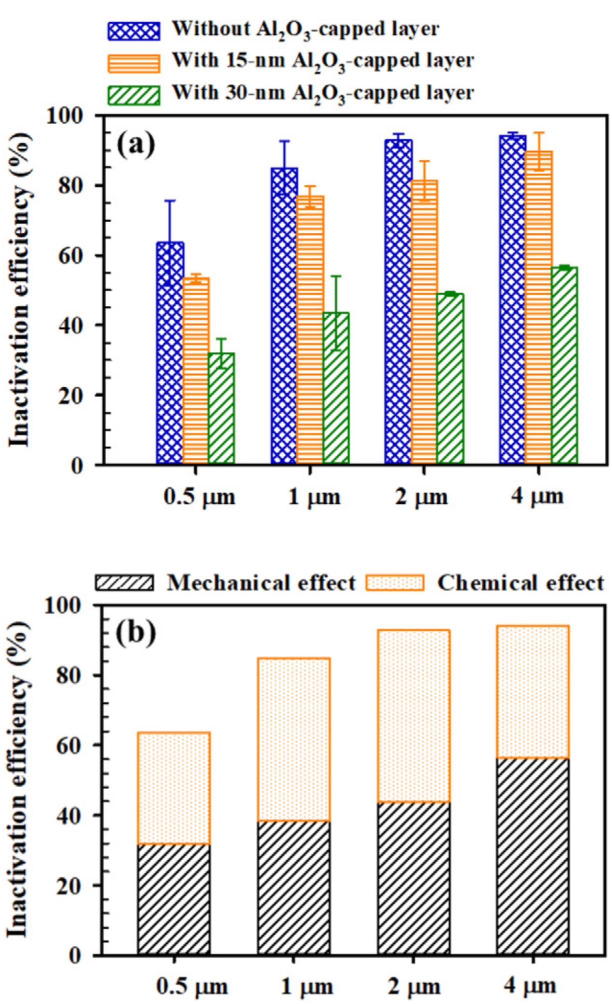

Fig. 7. (a) Inactivation efficiency of *E. coli* upon 30 min exposure to ZnO NR arrays of various lengths with different thicknesses of Al_2O_3 (capping) layers under dark conditions. (b) Quantitative analysis of influence factors for antibacterial activity of ZnO NR arrays.

3.6. Classification of the antibacterial activity mechanisms of ZnO NR arrays under dark conditions

The main factors associated with the antibacterial activity of ZnO NR arrays under dark conditions are summarized in Fig. 7(a). The pure ZnO NR arrays without Al_2O_3 layer exhibited a combinational effect for *E. coli* inactivation through the mechanical rupture and chemical deformation by ROS and zinc ions, reaching a maximum of 92.8% with the 2 μm tall ZnO NR array. The coated arrays with 15 nm thick Al_2O_3 layer, however, produced less ROS and zinc ions. As a result, the antibacterial activity of the 15 nm coated arrays was less influenced by chemical factors, resulting in a ~10% lower inactivation efficiency compared to that of the uncoated arrays for all lengths. With the thicker Al_2O_3 coating of 30 nm on the ZnO NR arrays, the chemical factors of the ROS and zinc ions were completely eliminated, implying that only the morphological effect, i.e., the physical rupture of *E. coli*, was responsible for bacterial inactivation, as it yielded 43.9% with 2 μm tall ZnO NR arrays. The controls in length and surficial coating over the ZnO NR arrays finally enabled quantitatively analyzing their antibacterial mechanisms, as redrawn in Fig. 7(b). The morphological effect for physical deformation of *E. coli* became dominant; the overall bactericidal activity increased from 31.9 to 56.4% as the length of the arrays increased from 0.5 to 4 μm tall. The chemical effect originated predominantly from ROS formation and marginally from zinc ion leaching, with the remaining 31.7 and 37.8% owing to the 0.5 and 4 μm tall ZnO NR arrays, respectively. Although both physical and chemical factors are known to affect the antibacterial activity of fabricated nanostructures, their actual share has not yet been quantitatively measured (Lakshmi Prasanna and Vijayaraghavan, 2015; Raghupathi et al., 2011). This study revealed that the antibacterial activity on 2 μm tall ZnO NR arrays under dark conditions is affected in the order of morphology (48.9%) > ROS production (40.9%) > released Zn^{2+} ions (3%).

3.7. Applications of ZnO NR arrays to real water samples for antibacterial treatment

To confirm the applicability of the antibacterial activity of ZnO NR arrays under an actual environment, antibacterial tests were conducted using drinking (bottled) and surface (pond) water. The antibacterial treatment of the water samples was confirmed using 2 μm tall ZnO NR arrays. In general, the performance of nanomaterials under realistic water treatment conditions is known to correlate to water quality parameters, especially organic matter owing to their scavenging effect of generated ROS (Chu et al., 2019; Sharma et al., 2015). As shown in Table S2, the water quality parameters demonstrated that bottled and pond water have similar conductivity, DO, and pH values, but the pond water sample showed a much higher TOC level and turbidity. After filtering the sampled water, *E. coli* was artificially spiked to perform the antibacterial evaluation of the ZnO NR arrays.

Fig. 8 displays the inactivation efficiency of *E. coli* following 30 min exposure of ZnO NR arrays under different light conditions (dark and UV irradiation). In the bottled water, a bacterial inactivation efficiency of 87.5% was achieved under dark conditions, whereas a slightly lower efficiency, 80.4%, was achieved in the pond water. Such a discrepancy in efficiencies can be ascribed to a higher level of organic substances in the pond water, which consumed the generated ROS under dark conditions, resulting in lower antibacterial activity (Brame et al., 2015; Maeng et al., 2015). When exposed to UV light illumination, however, almost 90% of antibacterial activities were obtained in both bottled and pond water, which may have resulted from the enhanced chemical effect due to more ROS production by the NR arrays. This can be strongly observed in the aforementioned ESR spectra, which show more intense formation of hydroxyl radicals under UV irradiation than that under dark conditions (Fig. 6(a) and (b)). The high antibacterial activity of ZnO NR arrays was confirmed even in the complex environments, proving the feasibility of the arrays for actual inactivation application.

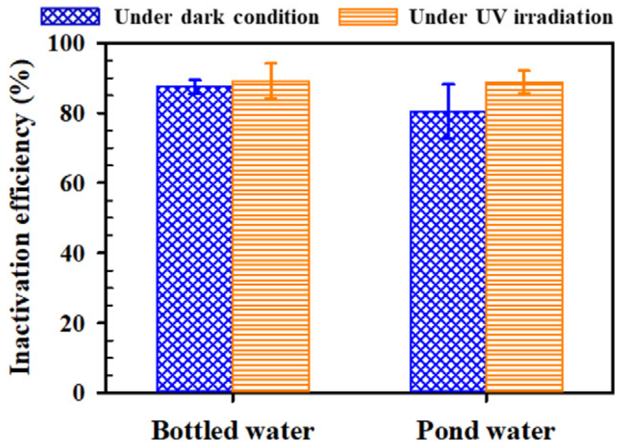

Fig. 8. Comparison of inactivation efficiency of 2 μm tall ZnO NR arrays under different conditions (dark conditions and UV irradiation) for *E. coli* in different water types (bottled and pond water) with 30 min of exposure.

4. Conclusion

The antibacterial activity of fabricated ZnO NR arrays under dark conditions was investigated from a mechanistic perspective. With NR arrays of various lengths, mechanical rupture of *E. coli* was predominant, showing higher inactivation efficiency with longer array lengths. The ZnO NR arrays were able to produce the ROS even under dark conditions owing to defect sites on the ZnO surface. When the ZnO NR arrays were coated with thick Al_2O_3 layers, the defects on ZnO were fully covered, producing no ROS in the environment. Considering that the chemical effect of ROS was not accounted for in these more thickly coated arrays, the mechanical effect arising from the ZnO NR array morphology was determined to be predominant. By comparing the uncoated and thickly coated ZnO NR arrays, the chemical inactivation by ROS formation and Zn^{2+} ions was further found to be a secondary effect. Therefore, the released Zn^{2+} ions from the ZnO NR arrays played a minor role in the antibacterial activity. Both coated and uncoated ZnO NR arrays can be applied in biomedical and antifouling fields where biofilm formation causes many problems even under dark conditions.

Declaration of competing interest

The authors declare that they have no known competing financial interests or personal relationships that could have appeared to influence the work reported in this paper.

Acknowledgments

This work was financially supported by the KIST institutional program (2E30510) and Korea Ministry of Environment as part of "The Eco-Innovation Program" (No. 2016000140006).

Appendix A. Supplementary data

Supplementary data to this article can be found online at https://doi.org/10.1016/j.scitotenv.2020.136574.

References

Akhavan, O., Ghaderi, E., 2010. Toxicity of graphene and graphene oxide nanowalls against bacteria. ACS Nano 4, 5731–5736.
Akhavan, O., Ghaderi, E., 2011. Copper oxide nanoflakes as highly sensitive and fast response self-sterilizing biosensors. J. Mater. Chem. 21, 12935–12940.
Akhavan, O., Mehrabian, M., Mirabbaszadeh, K., Azimirad, R., 2009. Hydrothermal synthesis of ZnO nanorod arrays for photocatalytic inactivation of bacteria. J. Phys. D. Appl. Phys. 42, 225305.
Amin, G., Asif, M., Zainelabdin, A., Zaman, S., Nur, O., Willander, M., 2011. Influence of pH, precursor concentration, growth time, and temperature on the morphology of ZnO nanostructures grown by the hydrothermal method. J. Nanomater. 2011, 5.
Applerot, G., Lipovsky, A., Dror, R., Perkas, N., Nitzan, Y., Lubart, R., Gedanken, A., 2009. Enhanced antibacterial activity of nanocrystalline ZnO due to increased ROS-mediated cell injury. Adv. Funct. Mater. 19, 842–852.
Bagchi, D., Rathnam, V.S., Lemmens, P., Banerjee, I., Pal, S.K., 2018. NIR-light-active ZnO-based nanohybrids for bacterial biofilm treatment. ACS Omega 3, 10877–10885.
Belver, C., López-Muñoz, M.J., Coronado, J.M., Soria, J., 2003. Palladium enhanced resistance to deactivation of titanium dioxide during the photocatalytic oxidation of toluene vapors. Appl. Catal. B 46, 497–509.
Bhadra, P., Mitra, M., Das, G., Dey, R., Mukherjee, S., 2011. Interaction of chitosan capped ZnO nanorods with *Escherichia coli*. Mater. Sci. Eng. 31, 929–937.
Brame, J., Long, M., Li, Q., Alvarez, P., 2015. Inhibitory effect of natural organic matter or other background constituents on photocatalytic advanced oxidation processes: mechanistic model development and validation. Water Res. 84, 362–371.
Chandel, N.S., McClintock, D.S., Feliciano, C.E., Wood, T.M., Melendez, J.A., Rodriguez, A.M., Schumacker, P.T., 2000. Reactive oxygen species generated at mitochondrial complex III stabilize hypoxia-inducible factor-1α during hypoxia a mechanism of O_2 sensing. J. Biol. Chem. 275, 25130–25138.
Chen, S., Guo, Y., Zhong, H., Chen, S., Li, J., Ge, Z., Tang, J., 2014. Synergistic antibacterial mechanism and coating application of copper/titanium dioxide nanoparticles. Chem. Eng. J. 256, 238–246.
Chu, L., Zhuan, R., Chen, D., Wang, J., Shen, Y., 2019. Degradation of macrolide antibiotic erythromycin and reduction of antimicrobial activity using persulfate activated by gamma radiation in different water matrices. Chem. Eng. J. 361, 156–166.
Colmenares, J.C., Luque, R., 2014. Heterogeneous photocatalytic nanomaterials: prospects and challenges in selective transformations of biomass-derived compounds. Chem. Soc. Rev. 43, 765–778.
George, S.M., 2009. Atomic layer deposition: an overview. Chem. Rev. 110, 111–131.
Groner, M., Fabreguette, F., Elam, J., George, S., 2004. Low-temperature Al_2O_3 atomic layer deposition. Chem. Mater. 16, 639–645.
Hirota, K., Sugimoto, M., Kato, M., Tsukagoshi, K., Tanigawa, T., Sugimoto, H., 2010. Preparation of zinc oxide ceramics with a sustainable antibacterial activity under dark conditions. Ceram. Int. 36, 497–506.
Huang, M.H., Mao, S., Feick, H., Yan, H., Wu, Y., Kind, H., Weber, E., Russo, R., Yang, P., 2001. Room-temperature ultraviolet nanowire nanolasers. Science 292, 1897–1899.
Jensen-Waern, M., Melin, L., Lindberg, R., Johannisson, A., Petersson, L., Wallgren, P., 1998. Dietary zinc oxide in weaned pigs—effects on performance, tissue concentrations, morphology, neutrophil functions and faecal microflora. Res. Vet. Sci. 64, 225–231.
Jiang, Y., Zhang, L., Wen, D., Ding, Y., 2016. Role of physical and chemical interactions in the antibacterial behavior of ZnO nanoparticles against *E. coli*. Mater. Sci. Eng. C. 69, 1361–1366.
Joe, A., Park, S.-H., Shim, K.-D., Kim, D.-J., Jhee, K.-H., Lee, H.-W., Heo, C.-H., Kim, H.-M., Jang, E.-S., 2017. Antibacterial mechanism of ZnO nanoparticles under dark conditions. J. Ind. Eng. Chem. 45, 430–439.
Kaimlová, M., Nemogová, I., Kolářová, K., Slepička, P., Švorčík, V., Siegel, J., 2019. Optimization of silver nanowire formation on laser processed PEN: surface properties and antibacterial effects. Appl. Surf. Sci. 473, 516–526.
Keem, K., Kim, H., Kim, G.-T., Lee, J.S., Min, B., Cho, K., Sung, M.-Y., Kim, S., 2004. Photocurrent in ZnO nanowires grown from Au electrodes. Appl. Phys. Lett. 84, 4376–4378.
Lakshmi Prasanna, V., Vijayaraghavan, R., 2015. Insight into the mechanism of antibacterial activity of ZnO: surface defects mediated reactive oxygen species even in the dark. Langmuir 31, 9155–9162.
Li, Q., Mahendra, S., Lyon, D.Y., Brunet, L., Liga, M.V., Li, D., Alvarez, P., 2008. Antimicrobial nanomaterials for water disinfection and microbial control: potential applications and implications. Water Res. 42, 4591–4602.
Liao, L., Lu, H., Li, J., He, H., Wang, D., Fu, D., Liu, C., Zhang, W.F., 2007. Size dependence of gas sensitivity of ZnO nanorods. J. Phys. Chem. C 111, 1900–1903.
Lipovsky, A., Nitzan, Y., Gedanken, A., Lubart, R., 2011. Antifungal activity of ZnO nanoparticles—the role of ROS mediated cell injury. Nanotechnology 22, 105101.
Liu, C., Kong, D., Hsu, P.-C., Yuan, H., Lee, H.-W., Liu, Y., Wang, H., Wang, S., Yan, K., Lin, D., Maraccini, P.A., Parker, K.M., Boehm, A.B., Cui, Y., 2016. Rapid water disinfection using vertically aligned MoS_2 nanofilms and visible light. Nat. Nanotechnol. 11, 1098.
Maeng, S.K., Cho, K., Jeong, B., Lee, J., Lee, Y., Lee, C., Choi, K.J., Hong, S.W., 2015. Substrate-immobilized electrospun TiO_2 nanofibers for photocatalytic degradation of pharmaceuticals: the effects of pH and dissolved organic matter characteristics. Water Res. 86, 25–34.
Moriarty, D., 1998. Control of luminous Vibrio species in penaeid aquaculture ponds. Aquaculture 164, 351–358.
Osonga, F.J., Kariuki, V.M., Yazgan, I., Jimenez, A., Luther, D., Schulte, J., Sadik, O.A., 2016. Synthesis and antibacterial characterization of sustainable nanosilver using naturally-derived macromolecules. Sci. Total Environ. 563-564, 977–986.
Polsongkram, D., Chamninok, P., Pukird, S., Chow, L., Lupan, O., Chai, G., Khallaf, H., Park, S., Schulte, A., 2008. Effect of synthesis conditions on the growth of ZnO nanorods via hydrothermal method. Physica B 403, 3713–3717.
Radke, L.L., Hahn, B.L., Wagner, D.K., Sohnle, P.G., 1994. Effect of abscess fluid supernatants on the kinetics of Candida albicans growth. Clin. Immunol. Immunopathol. 73, 344–349.
Raghupathi, K.R., Koodali, R.T., Manna, A.C., 2011. Size-dependent bacterial growth inhibition and mechanism of antibacterial activity of zinc oxide nanoparticles. Langmuir 27, 4020–4028.
Ramani, M., Ponnusamy, S., Muthamizhchelvan, C., Cullen, J., Krishnamurthy, S., Marsili, E., 2013. Morphology-directed synthesis of ZnO nanostructures and their antibacterial activity. Colloids Surf. B Biointerfaces 105, 24–30.

Sharma, V.K., McDonald, T.J., Kim, H., Garg, V.K., 2015. Magnetic graphene–carbon nanotube iron nanocomposites as adsorbents and antibacterial agents for water purification. Adv. Colloid Interf. Sci. 225, 229–240.
Shi, Y., Zhang, B., 2016. Recent advances in transition metal phosphide nanomaterials: synthesis and applications in hydrogen evolution reaction. Chem. Soc. Rev. 45, 1529–1541.
Song, W., Zhang, J., Guo, J., Zhang, J., Ding, F., Li, L., Sun, Z., 2010. Role of the dissolved zinc ion and reactive oxygen species in cytotoxicity of ZnO nanoparticles. Toxicol. Lett. 199, 389–397.
Sugarman, B., 1983. Zinc and infection. Rev. Infect. Dis. 5, 137–147.
Tam, K.H., Cheung, C.K., Leung, Y.H., Djurišić, A.B., Ling, C.C., Beling, C.D., Fung, S., Kwok, W.M., Chan, W.K., Philips, D.L., Ding, L., Ge, W.K., 2006. Defects in ZnO nanorods prepared by a hydrothermal method. J. Phys. Chem. B 110, 20865–20871.
Vayssieres, L., Keis, K., Lindquist, S.-E., Hagfeldt, A., 2001. Purpose-built anisotropic metal oxide material: 3D highly oriented microrod array of ZnO. J. Phys. Chem. B 105, 3350–3352.
Wenzel, R.N., 1949. Surface roughness and contact angle. J. Phys. Chem. 53, 1466–1467.
Yi, G., Li, X., Yuan, Y., Zhang, Y., 2019. Redox active Zn/ZnO duo generating superoxide ($\cdot O_2-$) and H_2O_2 under all conditions for environmental sanitation. Environ. Sci. Nano 6, 68–74.
Zhang, X., Qin, J., Xue, Y., Yu, P., Zhang, B., Wang, L., Liu, R., 2014. Effect of aspect ratio and surface defects on the photocatalytic activity of ZnO nanorods. Sci. Rep. 4, 4596.
Zhu, Q., Hu, X., Stanislaus, M.S., Zhang, N., Xiao, R., Liu, N., Yang, Y., 2017. A novel P/Ag/Ag_2O/Ag_3PO_4/TiO_2 composite film for water purification and antibacterial application under solar light irradiation. Sci. Total Environ. 577, 236–244.